Rethinking Doppler Effect for Accurate Velocity Estimation with Commodity WiFi Devices

Kai Niu, Xuanzhi Wang, Fusang Zhang, Rong Zheng, Zhiyun Yao, and Daqing Zhang, *Fellow, IEEE*

Abstract—**Enabling pervasive WiFi devices with non-contact sensing capability is an important topic in the field of integrated sensing and communication. Doppler effect has been widely exploited to estimate targets' velocity from wireless signals. However, the separation of signal sources and receivers complicates the relationship between Doppler frequency shift (DFS) and target velocity in WiFi-based non-contact sensing systems. In contrast to existing works that rely on either approximated relations or coarse-grained information such as whether a target is moving toward or away from WiFi transceivers, this paper investigates rigorously the dependency of velocity estimation accuracy on target locations and headings in WiFi sensing systems. The theoretical insights allow us to derive a closed-form solution and understand the fundamental limitation of velocity estimation. To optimize velocity estimation performance, we devise a receiving device selection scheme that dynamically chooses the optimal set of receivers among multiple available WiFi devices. A prototype real-time target tracking system has been implemented using commodity WiFi devices. Extensive experimental results show that the proposed system outperforms state-of-the-art approaches in velocity estimation and tracking, and is able to achieve $9.38cm/s$, $13.42°$, $31.08cm$ median errors in speed, heading and location estimation amongst experiments conducted in three indoor environments with three device placements and eight human subjects over 15 trajectories.**

Index Terms—**Doppler Frequency Shift, Velocity, WiFi Sensing, Tracking**

I. INTRODUCTION

To efficiently utilize congested spectrum resources, integrated sensing and communication (ISAC) has drawn increasing interest and attention in both academia and industry [1, 2, 3, 4, 5, 6, 7]. Among all the wireless communication techniques, WiFi devices have enjoyed pervasive deployments in home, commercial and enterprise environments nowadays. Beyond traditional communication functions, more and more works have recently integrated non-contact sensing capabilities into WiFi devices to enable a wide range of applications, from coarse-grained indoor positioning [8, 9, 10, 11] and activity recognition [12, 13, 14, 15, 16] to fine-grained vital sign monitoring [17, 18, 19, 20] and keystroke detection [21]. Such an integrated sensing and communication design [22, 23] makes it possible to fully exploit the limited spectrum of WiFi systems with low-cost hardware.

However, in contrast to mature information and communication theory for WiFi communication, the theory for WiFi sensing is still in its infancy. Only a few works investigate the principles and theoretical foundations of WiFi non-contact sensing systems. For instance, the Fresnel Zone model builds the mathematical relationship between waveform patterns of WiFi CSI (Channel State Information) and a target's position with respect to transceivers, motion trajectory [18, 19, 24, 25, 26]. The CSI-Speed model [13] is proposed to characterize the relation between Doppler Frequency Shift (DFS) and the rate of path length changes (also known as *Doppler speeds*) induced by moving targets. In reference [27], Niu *et al.* investigate the relationship between DFS and target's location, speed and motion direction to develop position-independent features for gesture recognition. These works help to understand the mechanisms behind WiFi sensing. But there still lack a set of mathematical models to concretely inform what leads to good or bad velocity estimation in WiFi sensing systems.

Estimating a target's velocity, namely, its speed and direction of motion (heading) is an important building block in many context-aware applications such as target tracking, gesture and activity recognition. Existing work that utilizes WiFi CSI in velocity estimation mainly falls into two categories. In the first category, building upon the insight that there exists a fixed relationship between Doppler speeds and the variations of CSI, researchers use Doppler speeds as surrogates for target speeds [13]. In fact, the two are not equivalent as revealed by several works [9, 27]. Heading estimation in some work of this category is limited to binary values, namely, whether a target is moving toward or away from WiFi transceivers used for sensing. In the second category, an approximate relation is established between Doppler speeds and target speed as in WiFiU [28] and QGesture [29] for gait and gesture recognition. However, all existing methods fail to shed lights on when velocity can be accurately estimated. To

K. Niu is with the Key Lab of High Confidence Software Technologies (Peking University), Ministry of Education, Beijing 100871, China, and also with the School of Computer Science, Peking University, Beijing 100871, China, and also with Beijing Xiaomi Mobile Software Co., Ltd., Beijing 100085, China (E-mail: xjtunk@pku.edu.cn).

X. Wang is with the Key Lab of High Confidence Software Technologies (Peking University), Ministry of Education, Beijing 100871, China, and also with the School of Computer Science, Peking University, Beijing 100871, China (E-mail:xuanzhiwang@stu.pku.edu.cn).

F. Zhang is with the State Key Laboratory of Computer Sciences, Institute of Software, Chinese Academy of Science, Beijing 100190, China, and also with State Key Laboratory for Novel Software Technology, Nanjing University, Nanjing, 210093, P.R China (E-mail: fusang@iscas.ac.cn).

R. Zheng is with the Department of Computing and Software, McMaster University, Hamilton, Ontario, L8S 4L8, Canada (E-mail: rzheng@mcmaster.ca).

Z. Yao is with the Key Lab of High Confidence Software Technologies (Peking University), Ministry of Education, Beijing 100871, China, and also with the School of Computer Science, Peking University, Beijing 100871, China (Email: zhiyunyao@stu.pku.edu.cn).

D. Zhang is with the Key Lab of High Confidence Software Technologies (Peking University), Ministry of Education, Beijing 100871, China, also with the School of Computer Science, Peking University, Beijing 100871, China, and also with the Telecom SudParis, Institut Polytechnique de Paris, 91011 Evry Cedex, France (E-mail: dqzhang@sei.pku.edu.cn, corresponding author).

the best of our knowledge, no prior theoretical analyses exist to examine under what circumstances velocity can be accurately estimated.

In this work, we consider the problem of target tracking in indoor environments with existing WiFi devices in home or enterprise settings. The targets are passive and do not emit any WiFi signals. Locations of WiFi transceivers are assumed to be known. We aim to answer the following questions: (1) can the velocity of a target be estimated equally well at all locations within the WiFi sensing coverage area? (2) As the placement of existing WiFi devices is uncontrollable in real world, how to select the optimal set of WiFi devices so that the target's velocity can be estimated as accurately as possible?

To answer both questions, we take a model-driven approach to velocity estimation. We first revisit the analytical relationship between DFS and target velocity, which gives rise a close-form solution to velocity estimation with one Tx and two Rx devices using DFS. We further perform a *sensitivity analysis* to mathematically characterize the effects of target location and heading on the accuracy of velocity estimation in relation to DFS errors. The analysis answers the first question and motivates the importance of WiFi device selection in target velocity estimation. Next, to answer the second question, a dynamic device selection algorithm is proposed to find the best set of Rxs among multiple randomly placed WiFi devices based on the theoretical analysis. A real-time target tracking system PITrack (Position-Independent Tracking) is implemented based on the proposed approaches and has been evaluated through extensive experiments in several real-world scenarios using commodity WiFi devices.

The main contributions of this work are summarized as follows:

(1) We perform a sensitivity analysis to characterize for the first time the dependency of *velocity estimation accuracy* on the heading and the location of a target in WiFi based sensing system, revealing that DFS measurement errors from WiFi receiving devices at different locations can yield different errors in velocity estimation.

(2) We design a scheme to dynamically select the best receivers among multiple WiFi devices to maximize velocity estimation accuracy for moving targets.

(3) We implement a prototype real-time target tracking system using commodity WiFi devices. Extensive experiments show the system outperforms state-of-the-art approaches and can achieve median errors of $9.38cm/s$ for moving speeds, $13.42°$ for moving directions, and $31.08cm$ for locations in a variety of indoor environments. A demo video of the prototype system can be found at: https://youtu.be/QGsM6N82rbw.

The rest of the paper is organized as follows. In Section II, we introduce the DFS-Velocity relation in WiFi sensing systems. In Section III, we establish the relation between CSI signals and DFS and mathematically analyze the sensitivity of velocity estimation with respect to DFS errors. The closed-form solution to velocity estimation from a single transmitter and two receivers and the algorithm for dynamic receiver selection are provided in Section IV. Section V describes the implementation of a target tracking system. Extensive experimental results are presented in Section VII. Section VIII discusses the limitations of the proposed approach and future work. We briefly review related work in Section IX and conclude the paper in Section X.

II. DOPPLER FREQUENCY SHIFTS IN WIFI SENSING SYSTEM

Doppler Effect is defined as the change in the frequency of a wave (e.g., sound, radio) caused by the relative motion of the wave source and an observer. *Doppler Frequency Shift* (DFS) is employed to quantify the frequency difference between signals at the observer and the source and is widely used to estimate target's velocity in sensing systems [30].

Unlike commonly used radars with co-located transceivers, WiFi-based non-contact sensing systems are bistatic, namely, signals transmitted by a WiFi Tx arrive at a separate WiFi Rx through multiple paths induced by objects in the surrounding environment. When a target moves, the frequency of the received WiFi signals changes due to the Doppler effect. The propagation of a signal reflected off a moving target with speed v and motion direction θ can be divided into two phases (Fig. 1): (1) *from the transmitter (Tx) to the moving target* and (2) *from the moving target to the receiver (Rx)*. Without loss of generality, we define a right-handed 2D coordinate system in the horizontal plane, whose origin is at Tx ($P_{Tx} = (0,0)$) and x-axis points toward Rx. Let $P_{Rx} = (LoS, 0)$ and $P_T^t = (x_T^t, y_T^t)$ be the location of Rx and the moving target at time t. The target moves at velocity $\vec{v}$ with magnitude v and heading θ. Angles of rotation are positive counterclockwise. For WiFi signals that propagate at the speed of light, both phases are subject to relativistic Doppler effects [31]. Specifically,
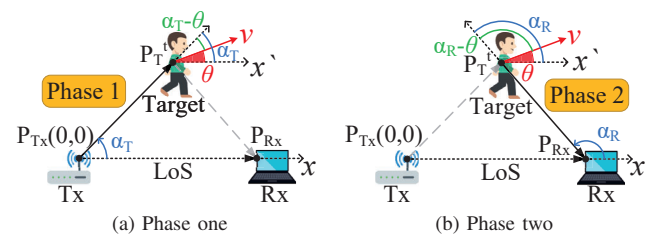

Fig. 1: Illustration of DFS-Velocity relation in WiFi based non-contact sensing system.

(1) *From Tx to the moving target:* As shown in Fig. 1a, the angle between $\vec{v}$ and the vector $P_T^t - P_{Tx}$ is given by $\alpha_T - \theta$, where α_T is the AoD (Angle of Departure) of the WiFi signal at Tx relative to the x-axis and can be calculated as $angle(P_T^t - P_{Tx})$ [1]. Based on the source reference frame of relativistic Doppler effects [31], the frequency of the signal arriving at the moving target is given by

$$f_{r1} = f_o \frac{1 - \beta cos(\theta - \alpha_T)}{\sqrt{1 - \beta^2}}, \qquad (1)$$

[1]For vector $\vec{a} = (x, y)$, $angle(\vec{a}) = arctan2\frac{y}{x}$ is the four-quadrant inverse tangent function.

where f_o is the source wave frequency, $\beta = v/c$ is the ratio between the speed of the target and the speed of light c.

(2) *From the moving target to Rx:* In the second phase, the signal reflected by the moving target continues to propagate to Rx as shown in Fig. 1b. The moving target can be viewed as a new signal source that transmits signals with frequency f_{r1}. The angle between $\vec{v}$ and the vector $P_T^t - P_{Rx}$ is $\alpha_R - \theta$, where α_R is AoA (Angle of Arrival) of the signal at Rx and can be calculated as $angle(P_T^t - P_{Rx})$. According to the observer reference frame of relativistic Doppler effect [32], the frequency of the received signal at Rx can be calculated as,

$$f_{r2} = f_{r1} \frac{\sqrt{1 - \beta^2}}{1 + \beta cos(\theta - \alpha_R)} = f_o \frac{1 - \beta cos(\theta - \alpha_T)}{1 + \beta cos(\theta - \alpha_R)}. \quad (2)$$

Therefore, the DFS induced by a moving target with movement speed v and heading θ in the WiFi-based sensing system is given by

$$f_D = f_{r2} - f_o = f_o \frac{-\beta cos(\theta - \alpha_T) - \beta cos(\theta - \alpha_R)}{1 + \beta(\theta - \alpha_R)}. \quad (3)$$
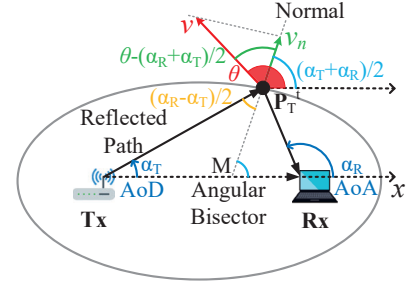
Under the assumption that the target's speed v is much less than the speed of light speed c, i.e., $\beta \ll 1$, Equation (3) can be simplified as

$$f_D = -\frac{f_o}{c} \cdot \underbrace{v cos(\theta - \frac{\alpha_R + \alpha_T}{2})}_{①} \cdot \underbrace{2 cos(\frac{\alpha_R - \alpha_T}{2})}_{②}. \quad (4)$$

The sign of DFS f_D indicates whether the movement of the target shortens (positive) or prolongs (negative) the reflected path from Tx to Rx. To understand the physical meaning of Equation (4), let us consider an ellipse with foci P_{Tx} and P_{Rx} that passes through P_T^t as illustrated in Fig. 2. Now, let M be a point on the segment $P_{Tx} P_{Rx}$ such that the line $P_T^t M$ is the angular bisector of $\angle P_{Tx} P_T^t P_{Rx}$. By the reflective property of ellipses [33], it can be proved that $P_T^t M$ coincides with the normal[2] of the ellipse at location P_T^t. Using geometry arguments, we can determine the various angles as depicted in Fig. 2. Two important observations are in order:

- *Term ① of Equation (4) projects the target's velocity to the normal direction of the ellipse at the target's location.* The projected speed $v_n = v cos(\theta - \frac{\alpha_R + \alpha_T}{2})$ depends on the target's heading θ and its location relative to the transceivers. At the same speed v, when the target moves along the normal direction (i.e., $\theta - \frac{\alpha_R + \alpha_T}{2} = 0°/180°$), DFS achieves its maximum absolute value. In contrast, when the target moves along the tangential direction of the ellipse (i.e., $\theta - \frac{\alpha_R + \alpha_T}{2} = 90°/-90°$), DFS is at its minimum absolute value 0.
- *Term ② of Equation (4) is the ratio between the rate of path length changes and the projected speed v_n.* Since the reflected path from Tx to Rx consists of two segments – the one from Tx to the target, and the one from the

(a) Mapping target's velocity to normal direction
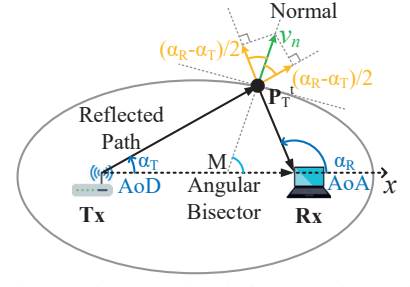
(b) Mapping normal velocity to path length change rate

Fig. 2: The physical meaning of DFS-Velocity relation.

target to Rx, path length changes can also be broken into the two parts. The rate of path length change is thus the sum of rates in two parts. Since the normal line is also the angular bisector of $\angle P_{Tx} P_T^t P_{Rx}$, the rates of path length changes along lines $P_{Tx} P_T^t$ and $P_T^t P_{Rx}$ induced by the normal velocity are both $v_n \cos \frac{\alpha_R - \alpha_T}{2}$. Therefore, the sum rate of changes is $2 v_n cos \frac{\alpha_R - \alpha_T}{2}$[3].

III. SENSITIVITY ANALYSIS OF VELOCITY ESTIMATION

In this section, we first discuss how to estimate DFS from WiFi CSI signals. Next, we mathematically analyze the sensitivity of speed and heading estimation in relation to DFS errors. Key properties are summarized to guide the selection of WiFi devices.

A. Estimating DFS from WiFi CSI

DFS induced by pedestrians or limb movements is typically in the range of tens of Hz in WiFi signals. This is much less than the 100kHz frequency drift between WiFi transceivers allowed by the IEEE 802.11n standard [13]. Thus, at the first glance, estimation of DFS from received signals is impossible. Fortunately, we find that DFS can be extracted directly from CSI, which is available from commercial-of-the-shelf devices [34]. Next, we will discuss the relationship between the two.

Firstly, consider a WiFi signal propagates through a static path such as the LoS path from Tx to Rx. Denote the single-tone signal transmitted as $X(f_o, t) = a e^{j2\pi f_o t}$ at time t, where f_o is the carrier frequency. The received signal through the

---

[2]The normal at a point on a curve is defined to be the line perpendicular to its tangent at the same point.

[3]Movements along the tangential directions of an ellipse do not change the total path length.

static path is given by $Y(f_o, t) = a'e^{j2\pi f_o(t-\tau_s)}$, where $\tau_s = l_s/c$ is the time delay on the static path of length l_s, a' is the attenuated signal magnitude. The CSI on this path is given by,

$$H_s(f_o, t) = \frac{Y(f_o, t)}{X(f_o, t)} = \frac{a'e^{j2\pi f_o(t-\tau_s)}}{ae^{j2\pi f_o t}} = Ae^{-j2\pi f_o\tau_s}, \quad (5)$$

where $A = a'/a$ is the amplitude of CSI. When a target moves in the environment, the reflected path changes with the target's location, called as *dynamic path*. Let τ_d be the time delay on the dynamic path at time t. The received signal through a dynamic path is given by $Y(f_r, t) = a''e^{j2\pi f_r(t-\tau_d)} = a''e^{j2\pi(f_o+f_D)(t-\tau_d)}$. Since $f_D \ll f_o$, the CSI for the dynamic path is given by,

$$H_d(f_o, t) = \frac{Y(f_r, t)}{X(f_o, t)} = \frac{a''e^{j2\pi(f_o+f_D)(t-\tau_d)}}{ae^{j2\pi f_o t}} \cong Ae^{j2\pi(f_D t - f_o\tau_d)}. \quad (6)$$

Equation (6) implies that the frequency of CSI induced by the dynamic path is the DFS caused by the corresponding moving target. CSI in practice is the linear superposition of channel responses from both static and dynamic paths, and thus can be represented as,

$$H(f_o, t) = \sum_{m \in P_S} A_m e^{-j2\pi f_o\tau_s^{(m)}} + \sum_{n \in P_D} A_n e^{j2\pi(f_{Dn}t - f_o\tau_d^{(n)})}, \quad (7)$$

where P_S is the set of static paths that correspond to zero DFS, and P_D is the set of dynamic paths that produce non-zero DFS. Furthermore, the frequency peaks in the Fourier transform of CSI correspond to the DFS of individual dynamic paths. Note that the relationship between DFS and CSI is still valid even if the Tx and Rx are separated by obstacles such as walls.

In practical systems, DFS estimations from CSI are error-prone. Short-time Fourier transform or Wavelet based methods are commonly adopted in DFS estimation [13, 28]. The accuracy of both algorithms is affected by the time window and the sampling rate used. Longer time windows lead to higher frequency resolutions but lower accuracy when targets change positions. Sample rates are fundamentally limited by the hardware used. However, as indicated in Equation (4), DFS in a WiFi-based non-contact sensing system is not only a function of the moving speed and heading direction of a target, but also depends on the location of the target. Therefore, given a fixed DFS error, the speed and heading estimates depend on the placement of the Tx and Rx with respect to the target. Next, we provide a sensitivity analysis of velocity estimation and its empirical evidence will be provided in Section VI.

B. Sensitivity Analysis of Speed Estimation

From Equation (4), the first-order derivative of the moving speed with respect to DFS is given by (see Appendix A for detailed derivations),

$$\frac{dv}{df_D} = -\frac{c}{f_o cos(\theta - \frac{\alpha_T+\alpha_R}{2}) \cdot 2cos\frac{\alpha_T-\alpha_R}{2}}. \quad (8)$$

The gradient is the ratio of changes in v and DFS. If f_D is an *unbiased* estimation of DFS, the larger the gradient, the more sensitive the speed estimation to DFS error. In other words, a small deviation in DFS can lead to a large error in v. Since the gradient term contains both the heading (θ) and the target location (α_T and α_R), we next analyze their effects separately.

- **Heading direction.** From Equation (8), we observe that the absolute value of the gradient is minimized (maximized), when $\theta - \frac{\alpha_T+\alpha_R}{2}$ equals 0° or 180° (90° or 270°) at a certain location. In other words, when the target moves along/opposite to the normal direction of the ellipse formed by Tx, Rx and the target at a location, the best speed estimation accuracy can be achieved. On the other hand, when the target moves along the tangential direction of the ellipse, the largest speed estimation errors follows. As illustrated in Fig. 3a, the accuracy decreases gradually from the normal direction to the tangential direction.
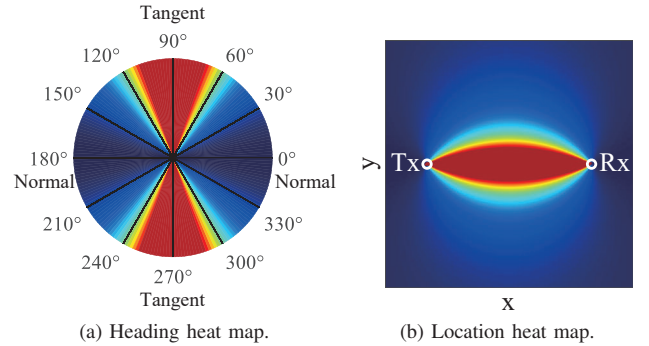

Fig. 3: Heat map for speed estimation accuracy. The blue color means high accuracy, while the red color means low accuracy.

- **Target location.** As discussed in Section II, the absolute value of the second term in Equation (4) is maximized when the target is on either end of the line that connects Tx and Rx or when the target is infinitely far away from Tx and Rx. The value is minimized when the target is on the LoS between Tx and Rx. As the target moves away from LoS, the absolute value of the second term increases. Accordingly, the accuracy of the speed estimation increases, as shown in Fig 3b.

From the above analysis, it is easy to show that among all possible locations and headings, speed estimation is the most precise when the target is at the far sides of the line that connects Tx and Rx, and moves along the line. In this situation, $\frac{dv}{df_D}$ equals $\frac{c}{2f_o}$. For example, when $f_o = 5.32GHz$, the accuracy of estimating moving speed is bounded by 2.82cm/s and 5.64cm/s for a DFS error of 1Hz and 2Hz, respectively. At any location other than those along LoS, the highest accuracy in speed estimation is achieved when the target moves along the normal direction of the ellipse induced by Tx, Rx and the target, and is given by $\frac{c}{2f_o cos\frac{\alpha_T-\alpha_R}{2}}df_D$. Note that the best accuracy is location dependent. For instance, the best accuracy at a location with 45° AoD and 135° AoA is 7.975cm/s for a DFS error of 2Hz.

C. Sensitivity Analysis of Heading Estimation

Similar to the analysis of moving speeds, we first take the derivative of heading θ with respect to DFS f_D as (see Appendix A),

$$\frac{d\theta}{df_D} = \frac{c}{v f_o sin(\theta - \frac{\alpha_T + \alpha_R}{2}) \cdot 2cos\frac{\alpha_T - \alpha_R}{2}}. \quad (9)$$

Since in Equation (9), the moving speed is user-dependent and its range is typically from 1.2m/s to 2.5m/s for pedestrians [35], the impact of moving speeds on the accuracy of heading estimation is not as significant as the heading (θ) and the target location (α_T and α_R), which will be discussed in more details next.

- **Heading direction.** When the target moves along the normal direction (i.e., $\theta - \frac{\alpha_T + \alpha_R}{2} = 0°$ or $180°$), the gradient is maximized. In other words, when the target moves along/opposite to the normal direction, the accuracy of heading estimation is the worst. In contrast, when the target moves along the tangential directions, the accuracy is maximized, as illustrated in Fig. 4. Note that this effect is exactly opposite to the case for speed estimation.
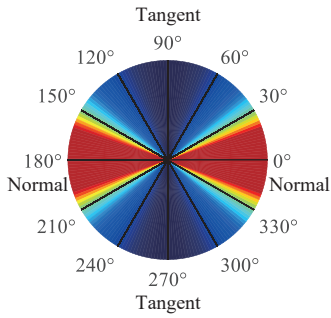

Fig. 4: Heat map for heading estimation accuracy as a function of target heading directions.

- **Target location.** The effect of target locations on the accuracy of heading estimation is the same as theirs on speed estimation. When a target moves away from LoS, the accuracy increases.

From the analysis, it is easy to show that among all possible locations and headings, heading estimation is the most precise and equals $\frac{cv}{2f_o}df_D$ when the target is at the far sides of the line that connects Tx and Rx and moves along the tangential directions. For instance, when f_o is $5.32GHz$ and the DFS error is 2Hz, the minimum heading estimation error is $4.846°$ at speed $1.5m/s$. At other locations, the highest accuracy in heading estimation is achieved when the target moves along the tangential direction of the ellipse induced by Tx, Rx and the target, and is given by $\frac{cv}{2f_o cos\frac{\alpha_T - \alpha_R}{2}}df_D$. For instance, the best accuracy at a location with $45°$ AoD and $135°$ AoA is $6.854°$ for a DFS error of 2 Hz.

D. Properties of Velocity Estimation

From the above sensitivity analysis, we summarize the properties of velocity estimation in WiFi-based non-contact sensing systems as follows:

(1) For both speed estimation and heading estimation, when the target moves away from the transceivers, the accuracy gradually increases. The best accuracy can be achieved on either end of the LoS of the transceivers.

(2) The accuracy of speed estimation *decreases* as a target changes its heading from the normal direction to the tangential direction of the ellipse induced by the Rx, Tx and the target. The opposite is true for heading estimation. The contradicting effect implies a trade-off exists between speed estimation and heading estimation.

(3) Among multiple randomly placed WiFi devices, as the location and heading of a target with respect to different Tx-Rx pairs varies, there exists an optimal Tx-Rx pair for velocity estimation, which changes as the target moves.

IV. DYNAMIC DEVICE SELECTION

Due to the coupling of target speed and heading, determining target velocity from Equation (4) requires at least one Tx and two Rxs. Fortunately, in indoor environments, WiFi devices are prevalent, making the estimation possible. However, as discussed in Section III, not all Tx-Rx pairs are equally good since the relative position and heading of a target to any Tx-Rx pair affect the accuracy of velocity estimation. In this section, we first provide a closed-form solution to estimate velocity from two pairs of Tx and Rx. Then, we present the rationale and the procedure to dynamically select the best pairs of transceivers as targets move.

A. Closed-form Solution for Velocity Estimation

Consider a single Tx and two Rxs. Let the AoD of WiFi signals from the Tx to the target be α_T. Denote the AoAs of the reflected signals at the two Rxs by α_{R1} and α_{R2}, respectively. Given f_{D1} and f_{D2}, i.e., the DFS at Rx1 and Rx2, we have,

$$\begin{cases} f_{D1} = -\frac{f_o}{c} \cdot vcos\left(\theta - \frac{\alpha_T + \alpha_{R1}}{2}\right) \cdot 2cos\frac{\alpha_T - \alpha_{R1}}{2}, \\ f_{D2} = -\frac{f_o}{c} \cdot vcos\left(\theta - \frac{\alpha_T + \alpha_{R2}}{2}\right) \cdot 2cos\frac{\alpha_T - \alpha_{R2}}{2}. \end{cases} \quad (10)$$

The system of equations can be solved directly (see Appendix B). In our implementation, we first calculate the heading as

$$\theta = \frac{\alpha_T + \alpha_{R1}}{2} + angle(\Phi_2 - \Phi_1 cos\frac{\Delta\alpha}{2}, \Phi_1 sin\frac{\Delta\alpha}{2}) \quad (11)$$

where $\Phi_1 = f_{D1}cos\frac{\alpha_T - \alpha_{R2}}{2}$, $\Phi_2 = f_{D2}cos\frac{\alpha_T - \alpha_{R1}}{2}$, $\Delta\alpha = \alpha_{R2} - \alpha_{R1}$, and $angle(a, b) = arctan2\frac{b}{a}$ is the four-quadrant inverse tangent function. The moving speed can then be solved as,

$$v = -\frac{cf_{D1}}{f_o cos(\theta - \frac{\alpha_T + \alpha_{R1}}{2}) \cdot 2cos\frac{\alpha_T - \alpha_{R1}}{2}}. \quad (12)$$

B. Scheme to Dynamically Select Optimal Receivers

As a target moves around in an environment, the best Tx-Rx pairs for speed estimation change over time. For the ease of presentation, we fix the Tx device and discuss how to select the best two Rx devices to minimize velocity estimation errors. The dynamic receiving device selection algorithm consists of three steps (Algorithm 1):

Algorithm 1: Algorithm for Dynamic Device Selection

Input: M: number of WiFi receivers; P_{Tx}: location of Tx; $P_{Rx}[1:M]$: locations of Rxs; P_T^{t-1}: estimated target's location at time $t-1$; θ_T^{t-1}: estimated target's heading at time $t-1$; $S_t[1:M]$: signal variance of Rxs at time t; $N_t[1:M]$: noise power of Rxs at time t; Ths_{SNR}: pre-defined threshold for Signal to Noise Ratio (SNR); Ths_r: pre-defined threshold for location

Output: $RxID_t$: IDs of selected Rxs at time t

1   $\alpha_T \leftarrow angle(P_T^{t-1} - P_{Tx})$;
2   **for** $i \leftarrow 1 : M$ **do**
3     $\alpha_R[i] \leftarrow angle(P_T^{t-1} - P_{Rx}[i])$;
4   **end**
5   $RxID_t \leftarrow$ Rx IDs of $S_t/N_t > Ths_{SNR}$; // select the Rxs with sufficient SNR.
6   **for** $j \leftarrow 1 : length(RxID_t)$ **do**
7     $r[j] \leftarrow |2cos(\frac{\alpha_T - \alpha_R[RxID_t[j]]}{2})|$;
8   **end**
9   $RxID_t \leftarrow$ Rx IDs of $r > Ths_r$; // select the Rxs whose LoSs are far away from the target.
10   **for** $k = 1 : length(RxID_t)$ **do**
11     $\gamma[k] \leftarrow |cos(\theta_T^{t-1} - \frac{\alpha_T + \alpha_R[RxID_t[k]]}{2}) \cdot sin(\theta_T^{t-1} - \frac{\alpha_T + \alpha_R[RxID_t[k]]}{2})|$
12   **end**
13   $RxID_t \leftarrow$ Rx IDs of $max(\gamma, 2)$; // select the two optimal Rxs with heading direction.

---

(1) We first exclude receiver devices that are outside the sensing area of Tx. Generally speaking, signals reflected by a human target are weak due to the high attenuation along the reflected path and the low reflectivity of human body. Obstructions in indoor environments can further reduce the received signal strength. Therefore, the sensing area around any Tx-Rx pair is much less than typical WiFi communication ranges. In our implementation, a pre-defined threshold is empirically chosen to remove the receivers that have low Signal to Noise Ratio (SNR) and thus poor sensing capability.

(2) Next, we compute $|2cos\frac{\alpha_T - \alpha_R}{2}|$ for all remaining Rxs and exclude those with values smaller than a pre-defined threshold. Geometrically, this implies that the distances from the target to the LoS between the Tx and remaining Rxs are sufficiently large. Recall Property 1 in Section III-D, the farther away the target is from the LoS between the Tx and a selected Rx, the better the speed and heading estimation accuracy is. We set the pre-defined threshold to 0.3 to remove receivers whose LoSs are too close to the target (as illustrated by the area colored in red in Fig. 11 and Fig. 13, where sensitivity changes sharply).

(3) Denote the set of remaining receiver devices by $\mathcal{R}$. Next, using the estimated heading θ_T^{t-1} and location P_T^{t-1} of the target at time $t-1$, we compute the following quality for each device in $\mathcal{R}$:

$$\gamma(\alpha_T, \alpha_R, \theta_T^{t-1}) = \left| cos\left(\theta_T^{t-1} - \frac{\alpha_T + \alpha_R}{2}\right) \cdot sin\left(\theta_T^{t-1} - \frac{\alpha_T + \alpha_R}{2}\right)\right|. \quad (13)$$

The two devices with the largest $\gamma(\alpha_T, \alpha_R, \theta_T^{t-1})$ are chosen. Their measurements are utilized in Equation (10) to solve for θ_t and v_t at current time t. With the newly estimated θ_t, we repeat this process until no further changes are made in device selection. Recall from the sensitivity analysis in Section III, we show that $\theta - \frac{\alpha_T + \alpha_R}{2}$ has a contradicting effect on the two gradients in Equation (8) and Equation (9). In other words, the two qualities cannot be maximized at the same time. As a trade-off, we instead find an α_R (or equivalently an Rx) such that $\left|cos\left(\theta_T^{t-1} - \frac{\alpha_T + \alpha_R}{2}\right) \cdot sin\left(\theta_T^{t-1} - \frac{\alpha_T + \alpha_R}{2}\right)\right|$ is large.

As an example, let us consider a smart home with WiFi-enabled television, table lamp and air conditioner as illustrated in Fig. 5a. The blue star represents a transmitter device such as a WiFi router, while the numbered green triangles are WiFi-enabled home appliances and can be used as receiving devices. In this example, there are one Tx and six Rxs. A target (indicated by a red dot) is on her way out of one bedroom in the upper right corner. In the setup, Rx6 is too far from the target and thus is excluded. For each of the remaining devices, if we draw a line between the device and the Tx and compare the distance from the target to the line, it can be observed that Rx2 yields a distance smaller than the pre-defined threshold. Therefore, Rx2 is removed from the candidate set. Finally, after comparing their respective γ values, Rx1 and Rx4 are selected as the final receiving devices, whose measurements will be used in solving Equation (10). When the target arrives at location 2 and walks toward the sofa, Rx2 is excluded as it is far away from the target. Rx1 is also removed since the target is too close to the LoS between Tx and Rx1. Finally, Rx4 and Rx5 with the largest γ are selected. When the target returns to the living room and passes by location 2 but with a different heading, Rx3 and Rx6 will be selected. This example shows that when the target is at different locations or moves in different directions, the dynamic selection algorithm will pick different sets of receivers for velocity estimation.

(a) Location 1   (b) Location 2 and heading 1   (c) Location 2 and heading 2
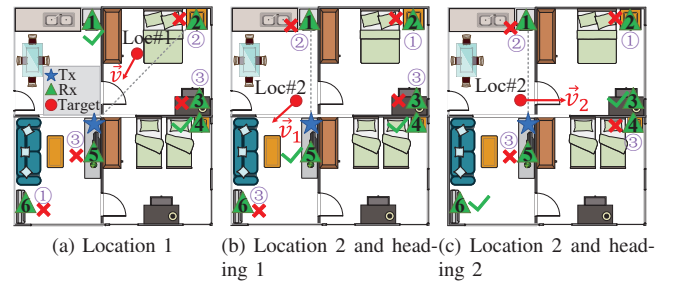
Fig. 5: A illustration of receiving device selection from multiple WiFi devices when a participant is at different locations or moves in different directions.

V. TRACKING SYSTEM IMPLEMENTATION

In this section, we design and implement a real-time target tracking system PITrack (Position-Independent Tracking) based on the proposed velocity estimation method. Fig. 6 shows the system diagram, which consists of three core modules: (1) data acquisition and preprocessing, (2) velocity estimation, and (3) trajectory reconstruction. Raw CSI data is collected from multiple devices and is filtered to remove phase offsets and amplitude noises. Once walking is detected, the system automatically selects two devices to extract DFS and estimate the target's velocity. Finally, combined with the initial position and velocity, its trajectory is determined. A video demo is available at: https://youtu.be/QGsM6N82rbw. Next, we will present the detailed implementation.
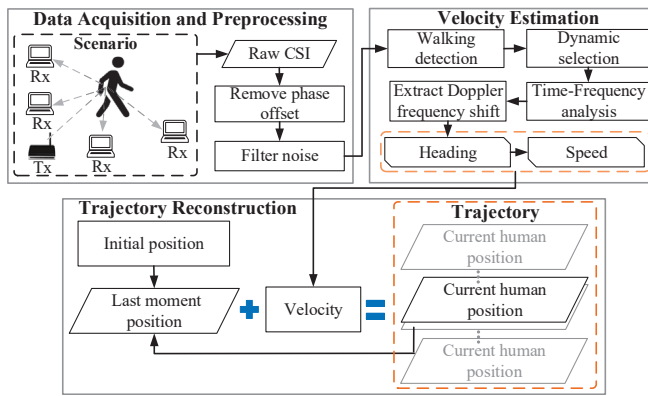
Fig. 6: System overview of PITrack.

(1) **Data acquisition and preprocessing.** Our system employs one WiFi transmitter and at least two WiFi receivers. The Tx can be a WiFi router, while the Rxs can be any smart device with a WiFi module such as smart TVs or indoor lights. In the implementation, we use GigaByte MiniPCs equipped with Intel 5300 WiFi cards as the transceivers. All Rxs simultaneously receive WiFi packets transmitted by the Tx and send CSI measurements to a laptop in real-time. The laptop processes the latest 1000 packets (i.e., 1s data) from each Rxs and matches their sequence numbers to estimate target location and velocity. Measurements in any lost packet at a receiver are imputed by those in the nearest received packet. Each Rx is equipped with three omnidirectional antennas that are 3cm apart. Since the CSIs from two antennas in the same WiFi card are subject to the same phase offsets caused by carrier frequency offsets and sampling frequency offsets, we compute their ratio to eliminate the phase offsets in raw CSIs. Next, a least-square smoothing filter named Savitzky-Golay filter [36] is applied to further denoise the resulting ratio signals.

(2) **Velocity estimation.** Since walking can induce pseudo-periodic signals, we compute the auto-correlation of CSI using the aggregate channel features (ACF) algorithm. The value of the first peak at non-zero delay is compared with a threshold (0.3 in our implementation) to detect the presence of walking movements. Once walking is

detected, the locations of Tx and Rxs, the last estimated target location, and the last estimated heading are used in the dynamic receiving device selection algorithm (Algorithm 1) to choose the best two Rx devices. CWT (Continuous 1-D Wavelet Transform) is then used to extract the time-frequency spectrogram from the smoothed CSI ratio signals of the selected Rx devices. DFS corresponds to the frequency with the maximum energy, from which we compute the current velocity analytically using Equation (10). In CWT, Morse wavelets are used [37]. The time-bandwidth product of Morse wavelets is set as 120. The minimum and maximum scales are automatically determined from the energy spread of the wavelets in frequency and time domains by MATLAB. Each octave in 2^j to 2^{j+1} ($j \in \mathbb{Z}$) is further discretized into 10 finer scales, i.e., $2^j, 2^{j+1/10}, 2^{j+2/10}, ..., 2^{j+1}$.

(3) **Trajectory reconstruction.** Given an initial position, the target's locations can be estimated with the estimated velocities from Step 2 over time, forming its trajectory. A Kalman filter can be applied to further smooth out the trajectory. To visualize the target's trajectory in real time, a user interface (UI) has been developed. As shown in Fig. 7, the UI mainly consists of two modules: real-time video and real-time trajectory. The video displays the current experimental setting captured by a camera. The real-time trajectory module shows the ground truth trajectory recorded by a HTC ViVe Cosmos device in blue and the calculated trajectory by the proposed approach in orange. The depth of the colors represents the magnitude of moving speeds. The dynamically selected Rx devices are indicated by red circles, with excluded WiFi devices occluded in the UI.
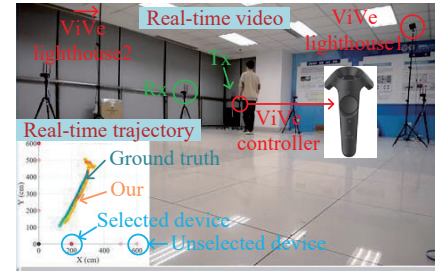

Fig. 7: User interface of PITrack.

VI. VALIDATION OF SENSITIVITY ANALYSIS

In this section, we conduct benchmark experiments to validate the sensitivity analysis of velocity estimation in Section III.

A. Experimental setup

As shown in Fig. 8, two GigaByte MiniPCs equipped with Intel 5300 WiFi cards are employed to collect CSI using CSI-Tool [34] and are placed 2m apart in an indoor environment. Each WiFi card is connected to three omnidirectional antennas. The receiver is configured to the monitor mode to capture packets from the transmitter at a sampling rate of 500Hz. A
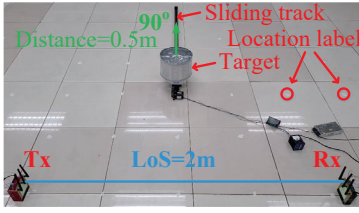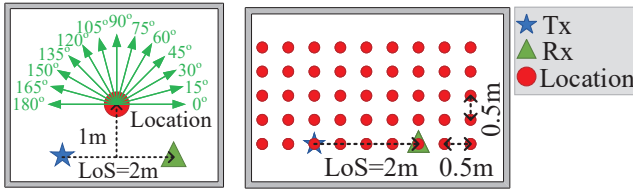
Fig. 8: Scenario of benchmark experiments.

metal cylinder is utilized to emulate a human target. The target and the transceivers' antennas are placed at the same height of 15cm. To precisely control the target's velocity, we use a sliding track to move it at a constant speed. DFS is estimated from CSI using the Continuous 1-D Wavelet Transform (CWT) algorithm, which is introduced in details in Section V.

To study the effect of different heading directions, we select an initial location on the perpendicular bisector of LoS and 1m away from LoS, as shown in Fig. 9a. The heading of the target varies from 0° to 180° at a step size of 15°. The target moves 0.5m in distance at the constant speed of $0.4m/s$ with the help of a sliding track. For each direction, the speed and heading at every CSI sample time are estimated using Equation (4), where the AoD and AoA in Equation (4) are calculated from the target's location.

(a) Setup for heading effect   (b) Setup for location effect

Fig. 9: Setup of benchmark experiments.

To investigate the effect of target locations, points on a $9 \times 5 = 45$ grid (red solid circles in Fig. 9b) are selected as initial target locations. The distance between adjacent grid points is 0.5m horizontally or vertically. At all locations, the target moves at speed $0.4m/s$ over distance 0.5m. Its heading is set to be the normal direction at each location (and thus the term ① in Equation (4) is $0.4m/s$). From the experimental results, we compute the median error of speed and heading estimation for each trajectory, and then use linear and quadratic interpolations to refine the space resolution from 0.5m to 0.1m.

B. Experimental results

Fig. 10 shows the errors of estimated speeds when the target moves at different directions. Clearly, the minimum median error (2.69cm/s) with the least variation happens when the object moves along the normal direction 90°. When the heading angle increases to 180°, the speed estimation accuracy decreases and the median error is 12.12cm/s. Fig. 11 shows the speed estimation errors at different locations with the normal heading. We observe that from the region around LoS outwards, estimation errors decrease rapidly, and then stabilize

after a certain distance. Thus, locations away from the LoS have lower speed estimation errors.
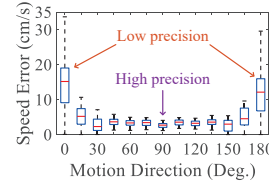

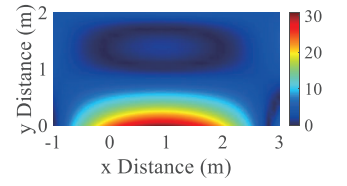Fig. 10: The effect of motion directions on moving speed estimation.

Fig. 11: The effect of target locations on moving speed estimation.

Fig. 12 shows the errors of estimated headings when the target is moving in different directions. Opposite to speed estimation, the minimum median error with the least variation occurs when the target moves in the tangential direction. Thus, one cannot simultaneously optimize speed and heading estimation performance. A trade-off needs to be made based on application requirements. Fig. 13 shows the errors of heading estimation for various locations. The results match well with the theoretical analysis in Section III-C.
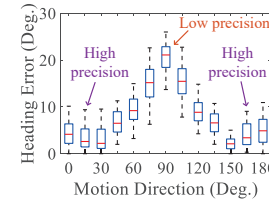

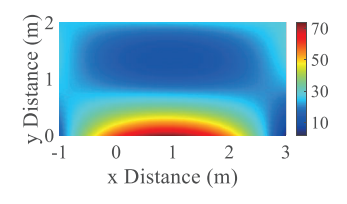Fig. 12: The effect of motion directions on heading estimation.

Fig. 13: The effect of target's location on heading estimation.

VII. TRACKING PERFORMANCE EVALUATION

In this section, we evaluate the performance of the proposed the target tracking system PITrack in several indoor scenarios using commodity WiFi devices. To evaluate the impact of dynamic receiving device selection, we also implement the approach described in Section V with fixed receiving devices. This approach is called PITrack w/o DS.

A. Experiment Setup

The hardware setup is identical to what was described in Section VI-A. We mount all transceivers on tripods. The height of transceivers is about 1.1m. The central frequency and bandwidth of transmitted signals are $5.32GHz$ and $40MHz$, respectively. The sensing area of the system is about 6m × 6m. The transmitter sends 1000 packets per second at a power level of 15dBm.

Test areas. As shown in Fig. 14, experiments are conducted in three typical indoor environments: a meeting room ($7.5m \times 9.8m$), a hall ($7.8m \times 8.4m$) and a corridor ($1.95m \times 8.4m$). One WiFi transmitter and six WiFi receivers are randomly deployed in the environments as labeled in Fig. 14. In the hall, we consider three different configurations for Tx and Rx locations,

indicated by green, blue and orange markers, respectively. Note that these three scenarios are representative of three types of indoor environments. Specifically, the meeting room is a multi-path rich environment, while the hall has few multipaths. The corridor corresponds to a non-LoS scenario where there exists blockage between the Tx and Rxs.
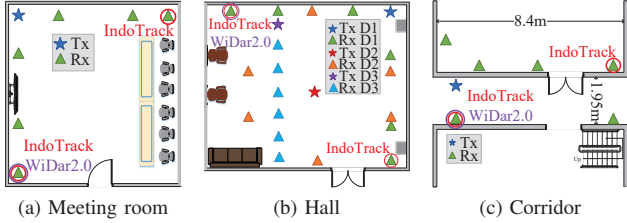

Fig. 14: Experimental setup in three indoor environments.

In the experiments, 8 participants have been recruited including six males and two females, aging from 20 to 32 with heights from $160cm$ to $190cm$ and weights from $47kg$ to $90kg$. The participants are asked to walk naturally at their own pace along 15 different trajectories of various shapes, including straight lines of different headings, circle, diamond, square, triangle and zigzag paths(Fig. 15)). Every user moves along each trajectory three times.
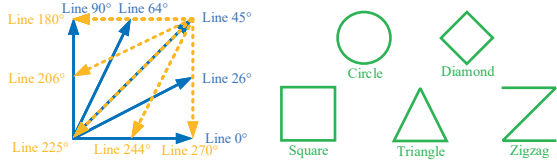

Fig. 15: 15 different trajectories for evaluation.

Ground truth. To obtain the ground truth trajectories and walking velocities, we employ HTC ViVe Cosmos that utilizes laser lights to localize and track targets for virtual reality applications [38, 39]. The sensing area of the HTC ViVe Cosmos system is $3.5m \times 3.5m$ with a tracking accuracy around $1.5mm$. Its sampling rate is 80Hz. We apply the nearest linear interpolation to upsample the measurements from HTC ViVe to make the sampling rate identical to that of CSI. During the experiments, each participant holds a ViVe controller (Fig. 7) in his/her hand to record ground truth locations. Walking velocities are then computed from the locations over time.
Baseline methods. We compare the proposed approach with two state-of-the-art methods, IndoTrack [9] and WiDar2.0 [10]. IndoTrack employs the MUSIC algorithm [40] to estimate the Doppler speed and its sign induced by a target at two receivers. It also estimates the angle of arrival (AoA) of the reflected signals for tracking. WiDar2.0 uses the Space Alternating Generalized Expectation Maximization (SAGE) algorithm [41] to concurrently estimate Doppler speed, AoA and time of flight, and then combines them to track targets. Stable AoA estimations heavily depend on the accurate phase information in CSI, which is difficult to obtain and requires labor-intensive calibration. As an alternative, we assume the availability of initial locations in two approaches as the case in

the proposed method for fair comparisons. Other parameters are set the same as recommendations in the authors' original source code implementations. The receiver devices used by IndoTrack and WiDar2.0 are shown in red and purple circles in Fig. 14, respectively.

B. Overall Performance

We first evaluate the overall performance of all three approaches in estimating moving speeds, headings and target tracking in three test areas and among different participants.

1) Movement Speed Estimation: Fig. 16 shows the cumulative distribution functions (CDFs) of speed estimation errors of the three approaches for all trajectories in three environments. In the hall, the Tx and Rxs are placed along the walls as indicated by green markers. From the figure, it can be observed that PITrack significantly outperforms IndoTrack and WiDar2.0. The median speed estimation errors of **PITrack, IndoTrack and WiDar2.0** are **$9.38cm/s$, $25.04cm/s$ and $41.72cm/s$** for walking speeds in $0m/s \sim 1.5m/s$, respectively. The low accuracy of IndoTrack can be attributed to the uneven distribution of speeds and headings at different locations. Since WiDar2.0 only uses one fixed transceiver pair, it is generally impossible for the pair to work well for all target locations. Furthermore, by comparing PITrack with and w/o DS, we can see the dynamic selection scheme can reduce the median error of speed estimation from $14.02cm/s$ to $9.38cm/s$.
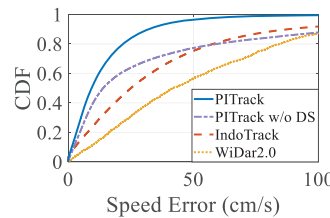

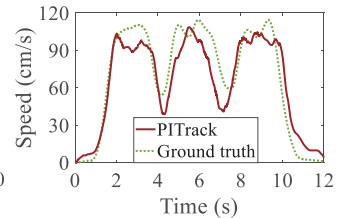Fig. 16: Overall speed accuracy.

Fig. 17: An example of speed estimation.

Fig. 17 illustrates the estimated and ground truth speeds as a participant walks along a triangular trajectory. The troughs around 60cm/s in both curves correspond to turns at the corners of the triangle while the maximum walking speeds of 1m/s are along the edges. We observe generally good agreements between the estimated speeds and the ground truth. PITrack is able to capture the changes in velocity with a mean estimation error of 11.9cm/s.

2) Heading Estimation: Next, we evaluate the accuracy of heading estimation. Fig. 18 shows the CDF of walking direction errors. Specifically, the median direction errors of **PITrack, IndoTrack, and WiDar2.0** are **$13.42°$, $31.26°$ and $29.09°$**, respectively. PITrack achieves the superior performance in part because WiFi receivers are selected dynamically as the target moves. Therefore, compared to the cases using fixed transmitter and receivers, our method is more resilient to weak signals from poorly positioned transceivers. As in speed estimation, the dynamic selection scheme can also
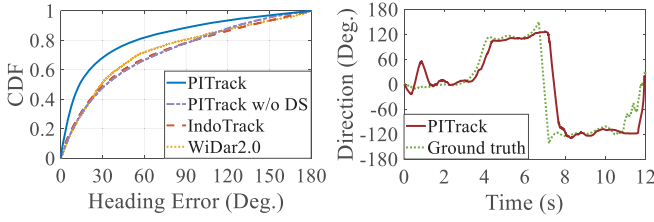
Fig. 18: Overall heading direction accuracy.

Fig. 19: An example of heading estimation.

significantly reduce the median error of heading estimation from 32.62° to 13.42°.

Fig. 19 illustrates the heading estimations from PITrack compared to ground truth values as a participant walks along a triangular trajectory over time. The two generally agree well. It should be noted that PITrack estimates the movement of the participant's torso while the ground truth values capture the participant's hand movements. As a result, there exist subtle bodily movements that are not captured by ViVe and the timings of turns can be different.

3) Target Tracking: In this set of experiments, participants are asked to walk along trajectories of different shapes (e.g., 'Z', triangle, rectangle, diamond and circle). Fig. 20a – Fig. 20e show the trajectories estimated by PITrack (red) compared to the ground truth (blue). Again, very good agreements can be observed. Fig. 20f compares the CDFs of different approaches. The median localization errors of **PITrack, Indo-Track and Widar2.0** are **31.08cm, 77.47cm and 118.08cm**, respectively. The performance of PITrack without dynamic selection scheme is only slightly better than IndoTrack, indicating the performance improvement of PITrack mainly comes from the dynamic selection scheme.

(a) 'Z'.   (b) Triangle.   (c) Rectangle.   (d) Diamond.

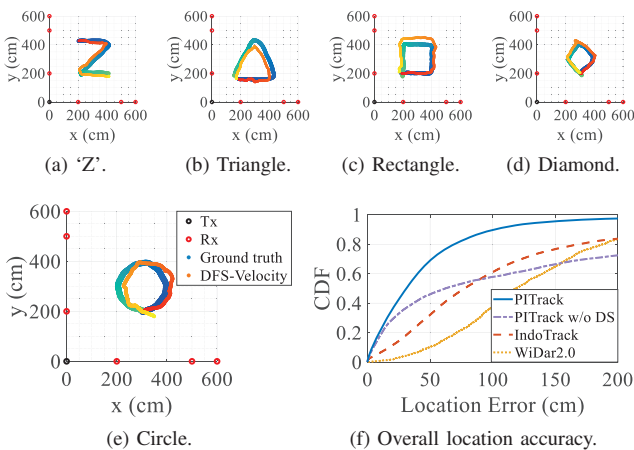(e) Circle.   (f) Overall location accuracy.

Fig. 20: Estimated trajectories and tracking performance. The ground truth trajectories start from blue and gradually change to green, while our trajectories start from red and gradually change to yellow.

C. Impacts of Experimental Setups

In this section, we study the performance of PITrack in different indoor environments, across different participants, as well as with different numbers of WiFi devices and their placements. This allows a better understanding of the robustness of the proposed approach across diverse settings.

1) Environment Changes: In the meeting room and hall, there exist line-of-sight paths between the Tx and all Rxs (Fig. 14). In contrast, the corridor is an example of non-line-of-sight (NLoS) through-wall scenarios.

Fig. 21 shows the speed estimation, heading estimation and tracking errors in the three environments. In the meeting room (M. room), the median errors of speed, heading and location estimates are $9.7cm/s$, $11.29°$, $29.19cm$ while in the hall and corridor, we have $9.59cm/s$, $13.06°$, $31.83cm$ and $7.21cm/s$, $29.04°$, $28.31cm$, respectively. Even though many objects in the meeting room such as tables and chairs create a multi-path rich environment (compared to the hall), the proposed approach achieves good performance. Furthermore, PITrack works equally well in the NLoS scenario where multiple WiFi receivers are deployed behind a wall in the corridor. This demonstrates the robustness of the proposed method in different environments.
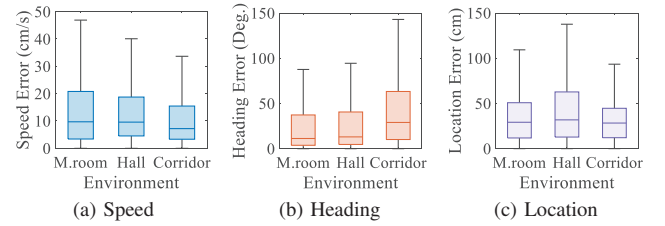

(a) Speed   (b) Heading   (c) Location

Fig. 21: Impact of environments on velocity estimation and tracking.

2) User Diversity: Fig. 22 shows the speed, direction and tracking errors among 8 participants. Although small variations across participants exist, the proposed approach performs consistently well with the standard deviations of the median errors of the three estimates at $1.71cm/s$, $1.55°$, $3.28cm$ across all participants. The results demonstrate that the proposed scheme is robust to a target's shape and size.

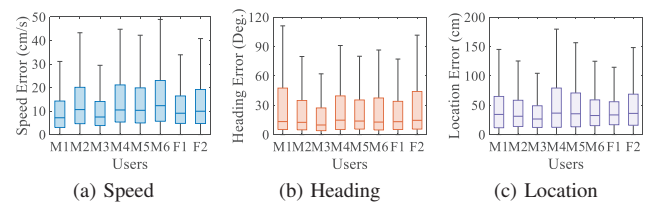(a) Speed   (b) Heading   (c) Location

Fig. 22: Impact of user diversity on velocity estimation and tracking.

3) Device Placement: Next, we investigate the impact of device placement. We consider three sets of receiver placements in the hall as shown in Fig. 14b. In the first setting (with Rxs indicated by green markers), the Rxs are deployed along the walls to mimic typical placements of home appliances and WiFi access points in households. The other two settings

correspond to uniformly circular placement (orange markers) and linear placement (blue markers), which are commonly used in WiFi sensing studies in literature. Fig. 23 shows the box graphs of speed, heading and location estimation errors. We can observe that the median errors of three placements are very similar. This is because regardless of the actual placement, the proposed method selects the optimal Rx devices to accurately estimate the target's speed and heading.
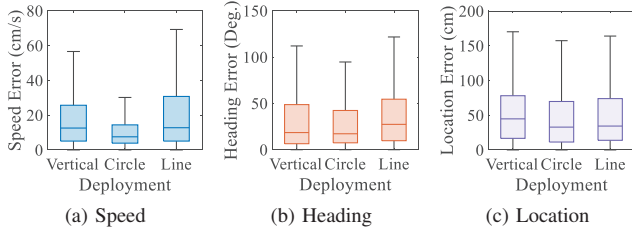

Fig. 23: Impact of device placement on velocity estimation and tracking.

4) Number of WiFi Devices: To understand the impact of the number of WiFi devices, we vary the number of Rxs from 2 to 6. Fig. 24 shows the estimation errors of three metrics decrease from $(20.40cm/s, 30.85°, 72.61cm)$ to $(8.82cm/s, 11.49°, 28.53cm)$. Furthermore, the standard deviation decreases as well. Clearly, more Rx devices lead to better accuracy and less variations since dynamic device selection can combat inferior performances caused by poorly placed devices. However, the improvement when the number of receiver devices goes beyond 4 is marginal. Therefore, the proposed system does not impose too much complexity in real-world deployment as it is reasonable to expect 4 or more WiFi-enabled appliance/devices in a typical home as long as they are sufficiently spaced.
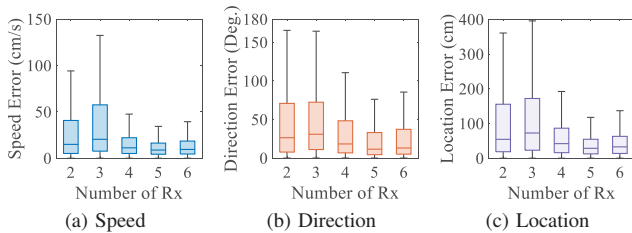

Fig. 24: Impact of the number of receiver devices on velocity estimation and tracking.

D. Irregular Trajectories in Multipath-rich Environments

To further demonstrate the system's performance in multipath-rich environments, we conduct additional experiments in another meeting room of size $5.1m \times 6.9m$ (Fig. 25a), where most of the space is occupied by furniture such as a big meeting table $(1.2m \times 2.4m)$, four desks, multiple chairs and so on. The transceivers are placed along the walls. Furthermore, to emulate irregular daily trajectories, a human target first walks from a location near the door to next to the upper-left corner of the meeting table and sits in the chair (as shown

in the blue track). Next, the subject gets up, walks to the window and closes it (red track), and then returns to the chair again (yellow track). Finally, the subject walks to the door and leaves the meeting room (purple track). The estimated trajectory is shown in Fig. 25b. We see that the system can indeed accurately reconstruct the irregular trajectory in the multipath-rich environment.
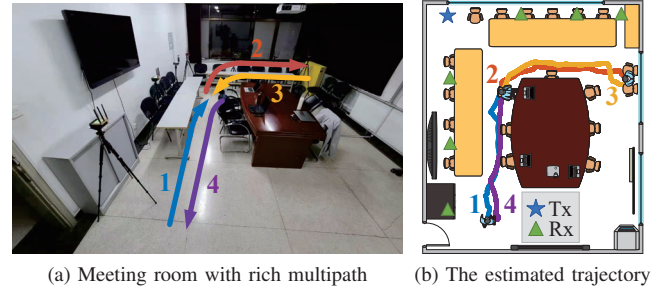

Fig. 25: Tracking irregular trajectories in a multipath-rich environment.

VIII. DISCUSSION

In the proposed target tracking system, although multiple WiFi receivers are needed to achieve accurate velocity estimation, the low time complexity of the closed-form solution and the dynamic selection scheme allow us to track targets in real time. Another limitation is the need for the initial locations of targets and the locations of transceivers to estimate target trajectories. In practice the transceivers are generally stationary and their locations only need to be measured once during deployments. The initial location of targets can be provided by users based on their relative positions to known indoor fixtures (e.g., doors). As part of future work, we plan to investigate joint estimation of target location and velocity in 3-D indoor scenarios with more devices available, and the applications of the proposed system in activity recognition and gesture recognition.

IX. RELATED WORK

In this section, we briefly review related work on RF-based non-contact velocity estimation and group them into two categories: WiFi-based and non-WiFi based approaches.

A. WiFi-based Velocity Estimation

Early work on WiFi-based motion sensing only estimates coarse-grained Doppler speed information instead of target velocity. For instance, WiSee [12] use the sign of Doppler speed, i.e. whether a target moves towards or away from the transceivers, to identify nine gestures with dedicated WiFi hardware. The same information is utilized in WiDance [42] to classify eight activities of a dancer's leg from commodity WiFi device measurements. However, the sign of Doppler speed is binary and does not correspond to real moving directions. WiDir [24] is among the first work that exploits multiple subcarriers to extract motion directions. However, it makes

the limiting assumption that the path length changes from two perpendicular WiFi receivers are orthogonal and thus can be used to approximate walking directions. Using a similar idea, FingerDraw [43] tracks the trajectory of a finger using two commodity WiFi devices. Doppler speed is also used directly to recognize activities such as walking, running and falling in CARM [13], and for step counting [44]. WiDar2.0 [10] and mD-Track [45] formulate Doppler speed estimation as a parameter estimation problem, and use the information in indoor tracking. However, since Doppler speed differs from the real speed of targets, the resulting tracking performance is unsatisfactory. As the DFS-Velocity relation in Section II reveals, the two are equal only when the second term in (4) is one.

WiFiU [28] and QGesture [29] calculate movement speeds as half of Doppler speeds in gait and gesture recognition. Such a relation clearly only holds in specific settings. WiSpeed [46] extracts moving speeds through a statistical electromagnetic approach without considering targets' moving directions. None of aforementioned work can accurately estimate the headings of moving targets. In more recent works such as IndoTrack [9], WiDar [47], WiVit [48] and WiDar3.0 [15], the authors recognize the dependency of DFS on target locations. Unfortunately, in lack of a rigorous theory, they fail to investigate when velocity can be accurately estimated and how to do so.

B. Velocity Estimation using Non-WiFi RF Signals

Other wireless technologies employed in velocity estimation include Doppler radar [49, 50, 51], FMCW radar [52, 53, 54, 55], UWB radar [56, 57, 58, 59], 4G/5G [60, 61, 62] and LoRa [63, 64, 65]. Using special-purposed Doppler radars, the authors in [66, 67, 68] exploit the relationship between the Doppler frequency and motion velocity to distinguish falls from other human activities. Taking advantage of high ranging resolutions, the authors of WiGait [52] use the FMCW radar developed by Adib et al. [69, 70] to estimate gait velocity and stride length from walking traces. UWB radars are also widely used to extract super-resolution Doppler velocities for through-wall imaging [71, 72] and gait identification [73, 74]. The afore-mentioned radar systems are monostatic with co-located transmitter and receiver. In such cases, the speed of a target is precisely half of the Doppler speed. This is no longer true in WiFi-based systems, where transceivers are separated. Bistatic radar systems [75, 76] have similar characteristics as WiFi-based systems. However, to the best of our knowledge, no prior analysis exists to quantify the dependency of velocity estimation accuracy on the headings and the locations of targets in bistatic radar systems or WiFi-based systems.

Recently, several works use commodity devices such as 4G/5G terminals and LoRa devices to extract motion information in a non-contact manner. Chen et al. [60] collect signals from 4G base stations and extract the Doppler speed induced by hand movements to recognize dynamic gestures. Gholampooryazdi et al. [61] develop a 5G prototype sensing system to estimate walking speeds. Zhang et al. [63] use LoRa devices to track target and observe the effect of different speeds on LoRa signals. The formula and analysis in this work are applicable to non-WiFi RF systems as well and can be used in conjunction with the aforementioned approaches to provide fine-grained motion information.

X. CONCLUSION

In this paper, we rigorously analyzed the effects of target location and heading on velocity estimation errors. We further proposed a dynamic receiver selection scheme to achieve accurate velocity estimation in non-contact sensing systems utilizing existing WiFi infrastructures. A close-form solution to velocity estimation was derived and has been implemented in a prototype system for real-time target tracking. Extensive experiments demonstrated the superior performance of the proposed system compared to state-of-the-art methods and its robustness under different settings. It should be noted that the proposed method is not limited to WiFi systems and can be applied to systems with spatially distributed RF transceivers such as 4G, 5G and LoRa networks as well. Furthermore, the theoretical analysis provides insights on when the target velocity can be accurately estimated, laying a solid foundation for the realization of integrated sensing and communication systems using WiFi devices.

APPENDIX A
DERIVATION OF SENSITIVITY ANALYSIS

From Equation (4), the first-order derivative of DFS with respect to the moving speed is given by

$$df_D = -\frac{f_o}{c}cos(\theta - \frac{\alpha_R + \alpha_T}{2}) \cdot 2cos(\frac{\alpha_R - \alpha_T}{2}) \cdot dv. \quad (14)$$

Moving dv from the right side to the left side of the equation and taking the reciprocal of both sides, we have the sensitivity of speed estimation

$$\frac{dv}{df_D} = -\frac{c}{f_o cos(\theta - \frac{\alpha_T + \alpha_R}{2}) \cdot 2cos\frac{\alpha_T - \alpha_R}{2}}. \quad (15)$$

Similarly, from Equation (4), the first-order derivative of DFS with respect to the heading direction of target is given by

$$df_D = \frac{f_o}{c} \cdot v sin(\theta - \frac{\alpha_R + \alpha_T}{2}) \cdot 2cos(\frac{\alpha_R - \alpha_T}{2})d\theta. \quad (16)$$

Therefore, the sensitivity of heading estimation is

$$\frac{d\theta}{df_D} = \frac{c}{v f_o sin(\theta - \frac{\alpha_T + \alpha_R}{2}) \cdot 2cos\frac{\alpha_T - \alpha_R}{2}}. \quad (17)$$

APPENDIX B
PROOF OF CLOSED-FORM SOLUTION

We can divide the formulas in Equation (10) and get

$$\frac{f_{D1}}{f_{D2}} = \frac{cos\left(\theta - \frac{\alpha_T + \alpha_{R1}}{2}\right) \cdot cos\frac{\alpha_T - \alpha_{R1}}{2}}{cos\left(\theta - \frac{\alpha_T + \alpha_{R2}}{2}\right) \cdot cos\frac{\alpha_T - \alpha_{R2}}{2}}. \quad (18)$$

Let $\Delta\alpha = \alpha_{R2} - \alpha_{R1}$. Equation (18) can be rewritten as

$$\frac{f_{D1}cos\frac{\alpha_T - \alpha_{R2}}{2}}{f_{D2}cos\frac{\alpha_T - \alpha_{R1}}{2}} = \frac{cos\left(\theta - \frac{\alpha_T + \alpha_{R1}}{2}\right)}{cos\left(\theta - \frac{\alpha_T + \alpha_{R1} + \Delta\alpha}{2}\right)}. \quad (19)$$

Let $\Phi_1 = f_{D1}cos\frac{\alpha_T - \alpha_{R2}}{2}$, $\Phi_2 = f_{D2}cos\frac{\alpha_T - \alpha_{R1}}{2}$, and $\beta = \theta - \frac{\alpha_T + \alpha_{R1}}{2}$. Equation (19) is further written as

$$\frac{\Phi_1}{\Phi_2} = \frac{cos\beta}{cos(\beta - \frac{\Delta\alpha}{2})}. \tag{20}$$

From Equation (20), we have

$$\Phi_1(cos\beta cos\frac{\Delta\alpha}{2} + sin\beta sin\frac{\Delta\alpha}{2}) = \Phi_2 cos\beta. \tag{21}$$

Furthermore, since

$$tan\beta = \frac{\Phi_2 - \Phi_1 cos\frac{\Delta\alpha}{2}}{\Phi_1 sin\frac{\Delta\alpha}{2}}, \tag{22}$$

β can be calculated as

$$\beta = angle(\Phi_2 - \Phi_1 cos\frac{\Delta\alpha}{2}, \Phi_1 sin\frac{\Delta\alpha}{2}), \tag{23}$$

where $angle(a, b) = arctan2\frac{b}{a}$ is the four-quadrant inverse tangent function.

Now the heading of the target is calculated as

$$\theta = \frac{\alpha_T + \alpha_{R1}}{2} + angle(\Phi_2 - \Phi_1 cos\frac{\Delta\alpha}{2}, \Phi_1 sin\frac{\Delta\alpha}{2}). \tag{24}$$

Finally, substituting θ in the first formula of Equation (10), the moving speed can then be solved as

$$v = -\frac{c f_{D1}}{f_o cos(\theta - \frac{\alpha_T + \alpha_{R1}}{2}) \cdot 2cos\frac{\alpha_T - \alpha_{R1}}{2}}. \tag{25}$$

ACKNOWLEDGMENT

REFERENCES

[1] F. Liu, C. Masouros, A. P. Petropulu, H. Griffiths, and L. Hanzo, "Joint radar and communication design: Applications, state-of-the-art, and the road ahead," *IEEE Transactions on Communications*, vol. 68, no. 6, pp. 3834–3862, 2020.

[2] X. Wang, J. Xu, A. Hassanien, and E. Aboutanios, "Joint communications with fh-mimo radar systems: An extended signaling strategy," in *ICASSP 2021 - 2021 IEEE International Conference on Acoustics, Speech and Signal Processing (ICASSP)*, 2021, pp. 8253–8257.

[3] L. Chen, F. Liu, W. Wang, and C. Masouros, "Joint radar-communication transmission: A generalized pareto optimization framework," *IEEE Transactions on Signal Processing*, vol. 69, pp. 2752–2765, 2021.

[4] D. Ma, N. Shlezinger, T. Huang, Y. Liu, and Y. C. Eldar, "Bit constrained communication receivers in joint radar communications systems," in *ICASSP 2021 - 2021 IEEE International Conference on Acoustics, Speech and Signal Processing (ICASSP)*, 2021, pp. 8243–8247.

[5] C. D'Andrea, S. Buzzi, and M. Lops, "Communications and radar coexistence in the massive mimo regime: Uplink analysis," *IEEE Transactions on Wireless Communications*, vol. 19, no. 1, pp. 19–33, 2020.

[6] G. Li, S. Wang, J. Li, R. Wang, X. Peng, and T. X. Han, "Wireless sensing with deep spectrogram network and primitive based autoregressive hybrid channel model," *arXiv preprint arXiv:2104.10378*, 2021.

[7] T. Zhang, S. Wang, G. Li, F. Liu, G. Zhu, and R. Wang, "Accelerating edge intelligence via integrated sensing and communication," *arXiv preprint arXiv:2107.09574*, 2021.

[8] X. Li, S. Li, D. Zhang, J. Xiong, Y. Wang, and H. Mei, "Dynamic-music: Accurate device-free indoor localization," in *Proceedings of the 2016 ACM International Joint Conference on Pervasive and Ubiquitous Computing*, 2016, p. 196–207.

[9] X. Li, D. Zhang, Q. Lv, J. Xiong, S. Li, Y. Zhang, and H. Mei, "Indotrack: Device-free indoor human tracking with commodity wi-fi," *Proc. ACM Interact. Mob. Wearable Ubiquitous Technol.*, vol. 1, no. 3, pp. 72:1–72:22, Sep. 2017.

[10] K. Qian, C. Wu, Y. Zhang, G. Zhang, Z. Yang, and Y. Liu, "Widar2.0: Passive human tracking with a single wi-fi link," in *Proceedings of the 16th Annual International Conference on Mobile Systems, Applications, and Services*, ser. MobiSys '18. New York, NY, USA: Association for Computing Machinery, 2018, p. 350–361.

[11] D. Wu, Y. Zeng, R. Gao, S. Li, Y. Li, R. C. Shah, H. Lu, and D. Zhang, "Witraj: Robust indoor motion tracking with wifi signals," *IEEE Transactions on Mobile Computing*, pp. 1–1, 2021.

[12] Q. Pu, S. Gupta, S. Gollakota, and S. Patel, "Whole-home gesture recognition using wireless signals," in *Proceedings of the 19th Annual International Conference on Mobile Computing and Networking*, ser. MobiCom '13. New York, NY, USA: Association for Computing Machinery, 2013, p. 27–38.

[13] W. Wang, A. X. Liu, M. Shahzad, K. Ling, and S. Lu, "Understanding and modeling of wifi signal based human activity recognition," in *Proceedings of the 21st annual international conference on mobile computing and networking*, 2015, pp. 65–76.

[14] H. Wang, D. Zhang, Y. Wang, J. Ma, Y. Wang, and S. Li, "Rt-fall: A real-time and contactless fall detection system with commodity wifi devices," *IEEE Transactions on Mobile Computing*, vol. 16, no. 2, pp. 511–526, 2017.

[15] Y. Zheng, Y. Zhang, K. Qian, G. Zhang, Y. Liu, C. Wu, and Z. Yang, "Zero-effort cross-domain gesture recognition with wi-fi," in *Proceedings of the 17th Annual International Conference on Mobile Systems, Applications, and Services*, ser. MobiSys '19. New York, NY, USA: ACM, 2019, pp. 313–325.

[16] R. Gao, M. Zhang, J. Zhang, Y. Li, E. Yi, D. Wu, L. Wang, and D. Zhang, "Towards position-independent sensing for gesture recognition with wi-fi," *Proc. ACM*

Interact. Mob. Wearable Ubiquitous Technol., vol. 5, no. 2, jun 2021.

[17] X. Liu, J. Cao, S. Tang, and J. Wen, "Wi-sleep: Contactless sleep monitoring via wifi signals," in *2014 IEEE Real-Time Systems Symposium*. IEEE, 2014, pp. 346–355.

[18] H. Wang, D. Zhang, J. Ma, Y. Wang, Y. Wang, D. Wu, T. Gu, and B. Xie, "Human respiration detection with commodity wifi devices: do user location and body orientation matter?" in *Proceedings of the 2016 ACM International Joint Conference on Pervasive and Ubiquitous Computing*, 2016, pp. 25–36.

[19] F. Zhang, D. Zhang, J. Xiong, H. Wang, K. Niu, B. Jin, and Y. Wang, "From fresnel diffraction model to fine-grained human respiration sensing with commodity wi-fi devices," *Proc. ACM Interact. Mob. Wearable Ubiquitous Technol.*, vol. 2, no. 1, Mar. 2018.

[20] Y. Zeng, D. Wu, J. Xiong, E. Yi, R. Gao, and D. Zhang, "Farsense: Pushing the range limit of wifi-based respiration sensing with csi ratio of two antennas," *Proc. ACM Interact. Mob. Wearable Ubiquitous Technol.*, vol. 3, no. 3, sep 2019.

[21] K. Ali, A. X. Liu, W. Wang, and M. Shahzad, "Keystroke recognition using wifi signals," in *Proceedings of the 21st annual international conference on mobile computing and networking*, 2015, pp. 90–102.

[22] A. Liu, Z. Huang, M. Li, Y. Wan, W. Li, T. X. Han, C. Liu, R. Du, D. T. K. Pin, J. Lu *et al.*, "A survey on fundamental limits of integrated sensing and communication," *arXiv preprint arXiv:2104.09954*, 2021.

[23] Q. Wu, J. Xu, Y. Zeng, D. W. K. Ng, N. Al-Dhahir, R. Schober, and A. L. Swindlehurst, "A comprehensive overview on 5g-and-beyond networks with uavs: From communications to sensing and intelligence," *IEEE Journal on Selected Areas in Communications*, pp. 1–1, 2021.

[24] D. Wu, D. Zhang, C. Xu, Y. Wang, and H. Wang, "Widir: Walking direction estimation using wireless signals," in *Proceedings of the 2016 ACM International Joint Conference on Pervasive and Ubiquitous Computing*, ser. UbiComp '16. New York, NY, USA: Association for Computing Machinery, 2016, p. 351–362.

[25] D. Zhang, H. Wang, and D. Wu, "Toward centimeter-scale human activity sensing with wi-fi signals," *Computer*, vol. 50, no. 1, pp. 48–57, 2017.

[26] F. Zhang, K. Niu, J. Xiong, B. Jin, T. Gu, Y. Jiang, and D. Zhang, "Towards a diffraction-based sensing approach on human activity recognition," *Proc. ACM Interact. Mob. Wearable Ubiquitous Technol.*, vol. 3, no. 1, Mar. 2019.

[27] K. Niu, F. Zhang, X. Wang, Q. Lv, H. Luo, and D. Zhang, "Understanding wifi signal frequency features for position-independent gesture sensing," *IEEE Transactions on Mobile Computing*, pp. 1–1, 2021.

[28] W. Wang, A. X. Liu, and M. Shahzad, "Gait recognition using wifi signals," in *Proceedings of the 2016 ACM International Joint Conference on Pervasive and Ubiquitous Computing*, ser. UbiComp '16. New York, NY, USA: Association for Computing Machinery, 2016, p.

363–373.

[29] N. Yu, W. Wang, A. X. Liu, and L. Kong, "Qgesture: Quantifying gesture distance and direction with wifi signals," *Proc. ACM Interact. Mob. Wearable Ubiquitous Technol.*, vol. 2, no. 1, Mar. 2018.

[30] V. C. Chen, *The micro-Doppler effect in radar*. Artech House, 2019.

[31] A. Einstein *et al.*, "On the electrodynamics of moving bodies," *Annalen der physik*, vol. 17, no. 10, pp. 891–921, 1905.

[32] T. P. Gill, *The Doppler effect: an introduction to the theory of the effect*. Academic Press, 1965.

[33] S. Berendonk, "Proving the reflective property of an ellipse," *Mathematics Magazine*, vol. 87, no. 4, pp. 276–279, 2014.

[34] D. Halperin, W. Hu, A. Sheth, and D. Wetherall, "Tool release: Gathering 802.11n traces with channel state information," *SIGCOMM Comput. Commun. Rev.*, vol. 41, no. 1, pp. 53–53, Jan. 2011.

[35] R. W. Bohannon, "Comfortable and maximum walking speed of adults aged 20—79 years: reference values and determinants," *Age and ageing*, vol. 26, no. 1, pp. 15–19, 1997.

[36] R. W. Schafer, "What is a savitzky-golay filter?[lecture notes]," *IEEE Signal processing magazine*, vol. 28, no. 4, pp. 111–117, 2011.

[37] J. M. Lilly and S. C. Olhede, "Generalized morse wavelets as a superfamily of analytic wavelets," *IEEE Transactions on Signal Processing*, vol. 60, no. 11, pp. 6036–6041, 2012.

[38] "Htc vive," https://www.vive.com/en/, 2020.

[39] V. Angelov, E. Petkov, G. Shipkovenski, and T. Kalushkov, "Modern virtual reality headsets," in *2020 International Congress on Human-Computer Interaction, Optimization and Robotic Applications (HORA)*. IEEE, 2020, pp. 1–5.

[40] R. Schmidt, "Multiple emitter location and signal parameter estimation," *IEEE transactions on antennas and propagation*, vol. 34, no. 3, pp. 276–280, 1986.

[41] J. A. Fessler and A. O. Hero, "Space-alternating generalized expectation-maximization algorithm," *IEEE Transactions on signal processing*, vol. 42, no. 10, pp. 2664–2677, 1994.

[42] K. Qian, C. Wu, Z. Zhou, Y. Zheng, Z. Yang, and Y. Liu, "Inferring motion direction using commodity wi-fi for interactive exergames," in *Proceedings of the 2017 CHI Conference on Human Factors in Computing Systems*, ser. CHI '17. New York, NY, USA: Association for Computing Machinery, 2017, p. 1961–1972.

[43] D. Wu, R. Gao, Y. Zeng, J. Liu, L. Wang, T. Gu, and D. Zhang, "Fingerdraw: Sub-wavelength level finger motion tracking with wifi signals," *Proc. ACM Interact. Mob. Wearable Ubiquitous Technol.*, vol. 4, no. 1, Mar. 2020.

[44] Y. Xu, W. Yang, J. Wang, X. Zhou, H. Li, and L. Huang, "Wistep: Device-free step counting with wifi signals," *Proc. ACM Interact. Mob. Wearable Ubiquitous Technol.*, vol. 1, no. 4, Jan. 2018.

[45] Y. Xie, J. Xiong, M. Li, and K. Jamieson, "Md-track: Leveraging multi-dimensionality for passive indoor wi-fi tracking," in *The 25th Annual International Conference on Mobile Computing and Networking*, ser. MobiCom '19. New York, NY, USA: Association for Computing Machinery, 2019.

[46] F. Zhang, C. Chen, B. Wang, and K. J. R. Liu, "Wispeed: A statistical electromagnetic approach for device-free indoor speed estimation," *IEEE Internet of Things Journal*, vol. 5, no. 3, pp. 2163–2177, 2018.

[47] K. Qian, C. Wu, Z. Yang, Y. Liu, and K. Jamieson, "Widar: Decimeter-level passive tracking via velocity monitoring with commodity wi-fi," in *Proceedings of the 18th ACM International Symposium on Mobile Ad Hoc Networking and Computing*, ser. Mobihoc '17. New York, NY, USA: Association for Computing Machinery, 2017.

[48] X. Li, D. Zhang, J. Xiong, Y. Zhang, S. Li, Y. Wang, and H. Mei, "Training-free human vitality monitoring using commodity wi-fi devices," *Proc. ACM Interact. Mob. Wearable Ubiquitous Technol.*, vol. 2, no. 3, Sep. 2018.

[49] M. Reznicek, "Doppler cw radar signal processing, implementation and analysis," in *2017 International Symposium ELMAR*, 2017, pp. 103–106.

[50] Y. Zhang, J. Wu, H. Sun, and T. Lu, "A novel multiple frequence cw system for messuring range and velocity," in *2016 CIE International Conference on Radar (RADAR)*, 2016, pp. 1–5.

[51] D. Kellner, M. Barjenbruch, J. Klappstein, J. Dickmann, and K. Dietmayer, "Tracking of extended objects with high-resolution doppler radar," *IEEE Transactions on Intelligent Transportation Systems*, vol. 17, no. 5, pp. 1341–1353, 2016.

[52] C.-Y. Hsu, Y. Liu, Z. Kabelac, R. Hristov, D. Katabi, and C. Liu, "Extracting gait velocity and stride length from surrounding radio signals," in *Proceedings of the 2017 CHI Conference on Human Factors in Computing Systems*, ser. CHI '17. New York, NY, USA: Association for Computing Machinery, 2017, p. 2116–2126.

[53] H. Zhou, P. Cao, and S. Chen, "A novel waveform design for multi-target detection in automotive fmcw radar," in *2016 IEEE Radar Conference (RadarConf)*, 2016, pp. 1–5.

[54] M. Ash, M. Ritchie, and K. Chetty, "On the application of digital moving target indication techniques to short-range fmcw radar data," *IEEE Sensors Journal*, vol. 18, no. 10, pp. 4167–4175, 2018.

[55] R. R. Monje, K. B. Cooper, R. J. Dengler, C. J. Cochrane, S. L. Durden, A. Tang, and M. Choukroun, "Long range-doppler demonstration of a 95 ghz fmcw radar," in *2018 15th European Radar Conference (EuRAD)*, 2018, pp. 409–412.

[56] Y. Sasaki, F. Shang, S. Kidera, T. Kirimoto, K. Saho, and T. Sato, "Three-dimensional imaging method incorporating range points migration and doppler velocity estimation for uwb millimeter-wave radar," *IEEE Geoscience and Remote Sensing Letters*, vol. 14, no. 1, pp. 122–126, 2017.

[57] M. Dawood, N. Quraishi, and A. V. Alejos, "Super-resolution doppler estimation using uwb random noise signals and music," *IEEE Transactions on Aerospace and Electronic Systems*, vol. 49, no. 1, pp. 325–340, 2013.

[58] T. Dogaru, "Doppler processing with ultra-wideband (uwb) radar revisited," US Army Research Laboratory Adelphi United States, Tech. Rep., 2018.

[59] R. Qi, X. Li, Y. Zhang, and Y. Li, "Multi-classification algorithm for human motion recognition based on ir-uwb radar," *IEEE Sensors Journal*, vol. 20, no. 21, pp. 12 848–12 858, 2020.

[60] W. Chen, K. Niu, D. Zhao, R. Zheng, D. Wu, W. Wang, L. Wang, and D. Zhang, "Robust dynamic hand gesture interaction using lte terminals," in *2020 19th ACM/IEEE International Conference on Information Processing in Sensor Networks (IPSN)*, 2020, pp. 109–120.

[61] B. Gholampooryazdi, I. Singh, and S. Sigg, "5g ubiquitous sensing: Passive environmental perception in cellular systems," in *2017 IEEE 86th Vehicular Technology Conference (VTC-Fall)*, 2017, pp. 1–6.

[62] R. S. A. Raja Abdullah, A. A. Salah, and N. E. Abdul Rashid, "Moving target detection by using new lte-based passive radar," *Progress In Electromagnetics Research*, vol. 63, pp. 145–160, 2015.

[63] F. Zhang, Z. Chang, K. Niu, J. Xiong, B. Jin, Q. Lv, and D. Zhang, "Exploring lora for long-range through-wall sensing," *Proc. ACM Interact. Mob. Wearable Ubiquitous Technol.*, vol. 4, no. 2, Jun. 2020.

[64] L. Chen, J. Xiong, X. Chen, S. I. Lee, K. Chen, D. Han, D. Fang, Z. Tang, and Z. Wang, "Widesee: Towards wide-area contactless wireless sensing," in *Proceedings of the 17th Conference on Embedded Networked Sensor Systems*, ser. SenSys '19. New York, NY, USA: Association for Computing Machinery, 2019, p. 258–270.

[65] F. Zhang, Z. Chang, J. Xiong, R. Zheng, J. Ma, K. Niu, B. Jin, and D. Zhang, "Unlocking the beamforming potential of lora for long-range multi-target respiration sensing," *Proc. ACM Interact. Mob. Wearable Ubiquitous Technol.*, vol. 5, no. 2, jun 2021.

[66] J. Hong, S. Tomii, and T. Ohtsuki, "Cooperative fall detection using doppler radar and array sensor," in *2013 IEEE 24th Annual International Symposium on Personal, Indoor, and Mobile Radio Communications (PIMRC)*, Sep. 2013, pp. 3492–3496.

[67] A. Gadde, M. G. Amin, Y. D. Zhang, and F. Ahmad, "Fall detection and classifications based on time-scale radar signal characteristics," in *Radar Sensor Technology XVIII*, vol. 9077. International Society for Optics and Photonics, 2014, p. 907712.

[68] L. R. Rivera, E. Ulmer, Y. D. Zhang, W. Tao, and M. G. Amin, "Radar-based fall detection exploiting time-frequency features," in *2014 IEEE China Summit International Conference on Signal and Information Processing (ChinaSIP)*, 2014, pp. 713–717.

[69] F. Adib, Z. Kabelac, D. Katabi, and R. C. Miller, "3d tracking via body radio reflections," in *11th USENIX Symposium on Networked Systems Design and Implemen-*
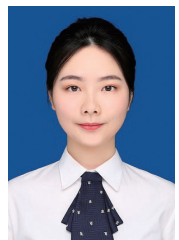
tation (NSDI 14).   Seattle, WA: USENIX Association, Apr. 2014, pp. 317–329.

[70] F. Adib, Z. Kabelac, and D. Katabi, "Multi-person localization via RF body reflections," in *12th USENIX Symposium on Networked Systems Design and Implementation (NSDI 15)*.   Oakland, CA: USENIX Association, May 2015, pp. 279–292.

[71] M. Setsu and S. Kidera, "Super-resolution doppler velocity estimation by gaussian-kernel based range-doppler conversion for uwb radar," in *2017 Progress in Electromagnetics Research Symposium - Fall (PIERS - FALL)*, 2017, pp. 1306–1311.

[72] M. Setsu, T. Hayashi, J. He, and S. Kidera, "Super-resolution doppler velocity estimation by kernel-based range– τ point conversions for uwb short-range radars," *IEEE Transactions on Geoscience and Remote Sensing*, vol. 58, no. 4, pp. 2430–2443, 2020.

[73] B. Lau, S. Haider, A. Boroomand, G. Shaker, J. Boger, and P. Morita, "Gait speed tracking system using uwb radar," 2018.

[74] S. P. Rana, M. Dey, M. Ghavami, and S. Dudley, "Non-contact human gait identification through ir-uwb edge-based monitoring sensor," *IEEE Sensors Journal*, vol. 19, no. 20, pp. 9282–9293, 2019.

[75] M. I. Skolnik, *Radar Handbook*.   McGraw-Hill Professional, 1990.

[76] N. J. Willis, *Bistatic radar*.   SciTech Publishing, 2005, vol. 2.

Fusang Zhang received the M.S. and Ph.D. degrees in computer science from the Institute of Software, Chinese Academy of Sciences, Beijing, China, in 2013 and 2017, respectively. He is currently an Associate Professor with the Institute of Software, Chinese Academy of Sciences. His current research interests include mobile and pervasive computing, ad hoc network, and wireless contactless sensing.

Rong Zheng received her Ph.D. degree from Dept. of Computer Science, University of Illinois at Urbana-Champaign and earned her M.E. and B.E. in Electrical Engineering from Tsinghua University, P.R. China. She is now a Professor in the Dept. of Computing and Software.
    Prof. Zheng's research interests include mobile computing, data analytics and networked systems. She is currently Canada Research Chair in Mobile Computing (Tier 1). She received the National Science Foundation CAREER Award in 2006, and was a Joseph Ip Distinguished Engineering Fellow from 2015-2018. She was recognized as having an established, superior research program that is highly rated in terms of originality and innovation, and was awarded the NSERC Discovery Accelerator Supplement in 2019.

Zhiyun Yao received the bachelor degree in computer science and technology from the School of Computer Science, Beijing University of Posts and Telecommunications, Beijing, China, in 2022. He is currently pursuing the Ph.D. degree in computer science with the School of Computer Science, Peking University, Beijing, China. His research interests include ubiquitous computing, mobile computing, wireless sensing, signal processing and software defined radio.

Kai Niu received the Ph.D. degree in computer software and theory from the School of Electronics Engineering and Computer Science, Peking University, Beijing, China, in 2021 and earned his M.E. degree in computer technology and B.E. degree in computer science and technology from the School of Electronic and Information Engineering, Xi'an Jiaotong University, Xi'an, China, in 2013 and 2016. He is now a joint postdoctoral fellow in Peking University, Beijing, China and Beijing Xiaomi Mobile Software Co., Ltd., Beijing, China. His current research interests include ubiquitous computing, wireless sensing and autonomous driving.

Daqing Zhang (Fellow, IEEE) is a Chair Professor with the Key Laboratory of High Confidence Software Technologies (Ministry of Education), School of Computer Science, Peking University, China, and Telecom SudParis, IP Paris, France. His research interests include context-aware computing, urban computing, mobile computing, big data analytics, pervasive elderly care, etc. He has authored more than 300 technical papers in leading conferences and journals. He received his Ph.D. degree from the University of Rome "La Sapienza", Italy, in 1996. He was the General or Program Chair for more than 17 international conferences, giving keynote talks at more than 20 international conferences. He is the Associate Editor for the IEEE Pervasive Computing, ACM Transactions on Intelligent Systems and Technology, and the Proceeding of ACM on Interactive, Mobile, Wearable and Ubiquitous Technologies. He is the winner of the Ten-Years CoMoRea Impact Paper Award at IEEE PerCom 2013 and Ten-Years Most Influential Paper Award at IEEE UIC 2019, the Honorable Mention Award at ACM UbiComp 2015 and 2016, and the Distinguished Paper Award at ACM UbiComp 2021.

Xuanzhi Wang received the bachelor degree in software engineering from the School of Software, Northwestern Polytechnical University, Xi'an, China, in 2020. She is currently pursuing the Ph.D. degree in computer science with the School of Electronics Engineering and Computer Science, Peking University, Beijing, China. Her current research interests include ubiquitous computing and mobile computing.